Nonstationary Internal Tides Observed Using Dual-Satellite Altimetry

E. D. ZARON

Department of Civil and Environmental Engineering, Portland State University, Portland, Oregon

(Manuscript received 28 January 2015, in final form 2 April 2015)

ABSTRACT

Dual-satellite crossover data from the *Jason-2* and *Cryosat-2* altimeter missions are used in a novel approach to quantify stationary and nonstationary tides from time-lagged mean square sea surface height (SSH) differences, computed for lags from 1 to 1440 h (60 days). The approach is made feasible by removing independent estimates of the stationary tide and mesoscale SSH variance, which greatly reduces the sampling error of the SSH statistics. For the semidiurnal tidal band, the stationary tidal variance is approximately 0.73 cm^2, and the nonstationary variance is about 0.33 cm^2, or 30% of the total. The temporal correlation of the nonstationary tide is examined by complex demodulation and found to be oscillatory with first 0 crossing at 400 h (17 days). Because a significant fraction of the time-variable mesoscale signal is resolved at time scales of roughly 150 h by the present constellation of satellite altimeters, the results suggest that it may be feasible to predict the nonstationary tide from modulations of the resolved mesoscale, thus enhancing the efficacy of tidal corrections for planned wide-swath altimeters such as the Surface Water and Ocean Topography (SWOT) mission.

1. Introduction

The internal tides are inertia-gravity waves that propagate within the ocean and are associated with subsurface currents and vertical isopycnal displacements, the magnitude of which depends on the strength of and proximity to the generation sites (Siedler 1991; Chiswell 2000; Rudnick et al. 2003). In spite of their origin from predictable astronomical forcing, in situ measurements of internal tides frequently exhibit substantial variability (Magaard and McKee 1973; Barnett and Bernstein 1975; Weisberg et al. 1987), which is attributed to refraction, Doppler shifting, and other interactions with the nontidal background (Rainville and Pinkel 2006; Klymak et al. 2008; Chavanne et al. 2010; Zilberman et al. 2011; Park and Farmer 2013).

The dynamics of internal tides may be described, approximately, in terms of horizontally propagating vertical modes that are the solution of a Sturm–Liouville problem, with the modes naturally ordered from fast to slow phase speed (Gill 1982). When the measurement technique permits separation of the first from the higher modes, a substantial fraction of the mode-1 signal is found to be stationary, that is, phase locked with the astronomical forcing. This fact has made it possible to observe internal tides in satellite measurements of sea surface height (SSH), which, because of the nature of the exact-repeat orbits employed, requires multiyear records to extract the stationary tides (Ray and Mitchum 1996; LeProvost 2001). Regional and global maps of the internal tides have been created using both empirical and dynamically constrained harmonic analysis, with higher spatial resolution achieved through combination of multiple missions (Dushaw et al. 2011; Zhao et al. 2011). Other techniques for isolating the low-mode internal tide include inverted echo sounders (Chiswell 2002), moored thermistor chains (Picaut et al. 1995), and acoustic travel time measurements (Dushaw et al. 1995).

There have been several efforts to determine the degree of phase locking and the partitioning of low-mode internal tide signals between the stationary and nonstationary parts. Ray and Zaron (2011) used two techniques to identify both the stationary and nonstationary internal tide from altimetry. The first approach was based on harmonic analyses of subsets of the data and comparison of tides within different

Denotes Open Access content.

Corresponding author address: E. D. Zaron, Department of Civil and Environmental Engineering, Portland State University, P.O. Box 751, Portland, OR 97207-0751.
E-mail: ezaron@pdx.edu

DOI: 10.1175/JPO-D-15-0020.1

epochs or seasons. Some regions of significant seasonal variability were identified; however, the resolution of nonstationarity by this technique is fundamentally constrained by the temporal sampling (once per 10 days for TOPEX/Poseidon and the Jason satellite series). The second approach utilized along-track wavenumber spectra to identify the SSH variance within wavenumber bands associated with internal tide modes. But because the internal tide field is spatially inhomogeneous and anisotropic, this approach may miss internal tide variance at wavenumbers that are unfavorably aligned with the satellite ground tracks. In situ measurements of the low-mode tide generally find nonstationary variance of between 20% and 30% of the stationary variance (Dushaw et al. 1995; Picaut et al. 1995; Chiswell 2002), but these values are representative of specific locations that tend to be located near generation sites.

The present paper takes a new approach in the time domain based on an analysis of dual-satellite crossover data. Data from the *Jason-2* (J2) and *Cryosat-2* (C2) missions are utilized because of the relatively high instrumental precision of the altimeters and the large number and spatial density of the orbit crossovers. A sample statistic, the mean square of J2 minus C2 SSH differences, is computed as a function of time lag and interpreted as a sum of instrumental noise and physical signals. In section 2, the sample statistic is defined and some of its properties are enumerated. In section 3, attributes of the internal tide are inferred and presented. Finally, sections 4 and 5 discuss and summarize the results.

2. Background

The quantity of interest is the mean square SSH difference between the J2 and C2 missions, binned by time lag τ_k, is

$$\hat{\Gamma}(\tau_k) = N_k^{-1} \sum_{ij} w_{ij}[\mathrm{J2}(t_i) - \mathrm{C2}(t_j)]^2 I_{ij,k}, \qquad (1)$$

where $\mathrm{J2}(t_i)$ and $\mathrm{C2}(t_j)$ are the SSH measured by the J2 and C2 missions at times t_i and t_j, respectively, and $I_{ij,k}$ is an indicator function that is equal to 1 if $\tau_k - \Delta t/2 \le |t_i - t_j| < \tau_k + \Delta t/2$ and the locations of the ith and jth observations are within 6 km (at orbit crossovers), and 0 otherwise. The quantity w_{ij} is a spatial normalization factor accounting for the unequal density of crossovers and ocean area as a function of latitude (Fig. 1), and it normalizes the sum so that $\hat{\Gamma}(\tau)$ corresponds to an area average. The normalization $N_k = \sum_{ij} I_{ij,k}$ equals the number of crossovers within each hourly bin of width $\Delta = 1$ h. The altimeter data are from the period 1 January 2010 to 30 May 2014, and N_k ranges from 4974 to 5369.

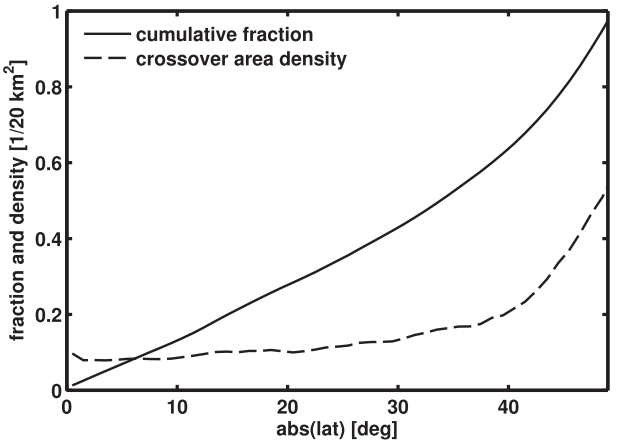

FIG. 1. The distribution of orbit crossovers as a function of latitude. The cumulative fraction of crossover locations as a function of latitude (solid line) illustrates the unequal distribution of crossover points, which if not accounted for, would lead to a geographic bias of the $\hat{\Gamma}$ statistic. In combination with the poleward convergence of the meridians, this effect leads to an unequal area density of crossover points (dashed line). For the purpose of display, the area density of crossovers is presented in units of crossovers per 20 km^2. The spatial normalization factor in (1), w_{ij}, is proportional to the inverse of the area density displayed.

The quantity $\hat{\Gamma}(\tau_k)$ is analogous to a variogram in spatial statistics, and it may be expressed alternately in terms of the lagged autocovariances and cross covariances of the J2 and C2 data. Second-order statistics of either two-point or two-time differences are referred to as *structure functions* in the fluid dynamics literature, and that terminology for $\hat{\Gamma}$ shall be used here (Frisch 1995). The data used to compute the structure function (1) consist of the 1-Hz measurements and environmental corrections extracted from the Radar Altimetry Database System (RADS; Naeije et al. 2002), utilizing the Geophysical Data Record, version D (GDR-D), standard (Picot et al. 2014). Because the ocean tidal correction from the Global Ocean Tide 4.10 (GOT4.10) model has been applied, nearly all variance associated with the stationary barotropic tide is removed (Stammer et al. 2014). To further reduce contamination by tide model and environmental corrections errors, data are restricted to come from within ±55° latitude in water deeper than 3000 m and be more than 60 km from the coast.

The uncertainty of the structure function may be computed from the expected error of the sample variance (Casella and Berger 2002, p. 257),

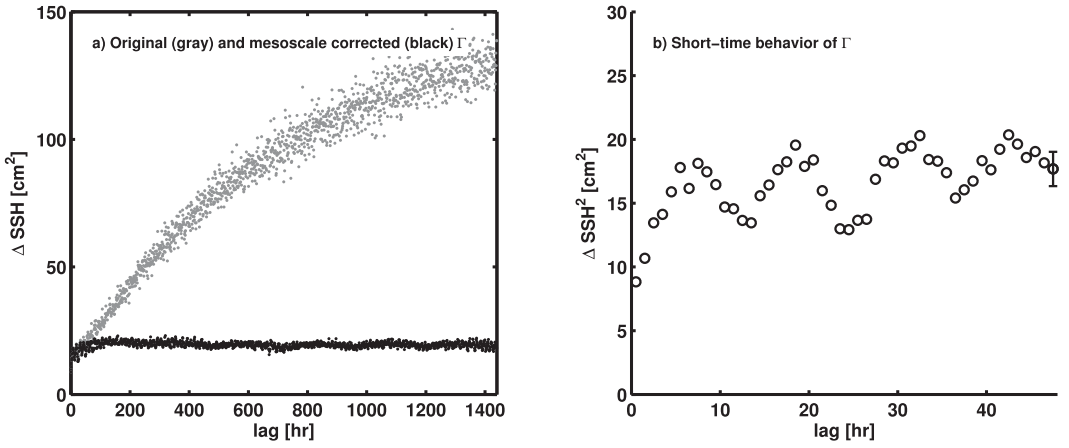

FIG. 2. Behavior of $\hat{\Gamma}(\tau)$ and $\Gamma(\tau)$. (a) Removal of the mesoscale signal from the SSH structure function $\hat{\Gamma}(\tau)$ (gray) leaves much smaller and less noisy values for subsequent analysis of $\Gamma(\tau)$ (black). (b) The behavior of $\Gamma(\tau)$ for $0 \le \tau \le 48$ h shows a rapid rise over about 6 h, followed by oscillations of approximately a 12-h period. Standard errors are similar at all lags and are shown for $\tau = 48$ h.

$$\sigma^2_{\Gamma}(\tau_k) = N_k^{-1}\left[\mu(\tau_k) - \frac{N_k - 3}{N_k - 1}\Gamma^2(\tau_k)\right], \qquad (2)$$

where the quantity $\mu(\tau_k)$ is the fourth moment of the SSH increments at lag τ_k,

$$\mu(\tau_k) = N_k^{-1}\sum_{ij}[\mathrm{J2}(t_i) - \mathrm{C2}(t_j)]^4 I_{ij,k}. \qquad (3)$$

The structure function is shown over the full range of τ_k from 1 to 1440 h (60 days) in Fig. 2. Because the sample error grows with signal variance, it is imperative to remove as much variance as possible before computing $\hat{\Gamma}(\tau)$. Furthermore, the distribution of SSH increments is increasingly wide-tailed for increasing τ_k, which makes σ^2_{Γ} too large to analyze $\hat{\Gamma}$ at long lags. To reduce the influence of nontidal SSH variance, consider the structure function in which the mesoscale signal $\mathbf{h}(\mathbf{x}_i, t_i)$ is removed (Ray and Byrne 2010):

$$\Gamma(\tau_k) = N_k^{-1}\sum_{ij} w_{ij}\{[\mathrm{J2}(t_i) - \mathbf{h}(\mathbf{x}_i, t_i)] - [\mathrm{C2}(t_j) - \mathbf{h}(\mathbf{x}_i, t_i)]\}^2 I_{ij,k}, \qquad (4)$$

where $\mathbf{x}$ indicates the spatial (latitude–longitude) coordinates. The mesoscale SSH field $\mathbf{h}(\mathbf{x}, t)$ used here is the merged multisatellite gridded absolute dynamic topography Ssalto/Duacs L4 product, version 5.0 (http://www.aviso.altimetry.fr), which is derived by objective mapping of data from the entire constellation of altimeter missions (LeTraon et al. 1998).

The mesoscale-corrected structure function $\Gamma(\tau)$ is less than $\hat{\Gamma}(\tau)$ at all lags (Fig. 2a), and the distribution of mesoscale-corrected SSH increments is nearly Gaussian (not shown), so the expected error of Γ is both reduced and varies little with τ compared to the expected error of $\hat{\Gamma}$. The Γ function shows several interesting features. Whereas $\hat{\Gamma}$ increases over the entire range of lags considered, Γ rises to a peak value of about 30 cm^2 at $\tau_* = 157$ h. Thus, the mesoscale $\mathbf{h}(\mathbf{x}, t)$ field apparently captures the SSH variance at time scales longer than τ_*. Second, the Γ function contains an oscillation with a period of 240 h (10 days), the orbit repeat time of J2, barely discernable at the scale of Fig. 2a. Third, there is a slight negative trend in Γ, the reason for which is unknown. Last, there are oscillations in Γ, apparent in Fig. 2b, with a period near twice per day (semidiurnal). It is these oscillations that shall be the focus of the analysis below.

Figure 2b illustrates the quantity $\Gamma(\tau)$ for τ ranging from 1 to 48 h. A smooth curve drawn through $\Gamma(\tau)$ would intercept the y axis at approximately 8.6 cm^2, which is consistent with the sum of the SSH variance attributed to waveform tracker noise in the two missions, plus radial orbit error. The linear rise from 0- to 5-h lag is consistent with a first-order autoregressive process that is hypothesized to be related to the decorrelation of reflectors (sea swell) within the nominal 6-km-radius patch of the ocean surface contributing to the radar return.

When there is tidal variability present, the expected form of $\Gamma(\tau)$ may be computed by considering a time series,

$$h(t) = A[1 + \alpha(t)]\cos[\omega t + \phi(t)], \qquad (5)$$

which represents a tide with mean amplitude A modified by (nondimensional) amplitude modulations $\alpha(t)$

and phase modulations $\phi(t)$. Under the assumption that both α and ϕ are uncorrelated and stationary Gaussian random variables, it is a straightforward exercise to derive the following expression for the expected value of the structure function, $\gamma(\tau) = \langle [h(t+\tau) - h(t)]^2 \rangle$:

$$\gamma(\tau)/A^2 = [1 - \cos(\omega\tau)]\left(1 + \frac{3\sigma_\phi^4}{4}\right) + [\sigma_\phi^2 - C_{\phi,\phi}(\tau)]\cos(\omega\tau) + [\sigma_\alpha^2 - C_{\alpha,\alpha}(\tau)\cos(\omega\tau)] - \frac{1}{2}\left(\sigma_\alpha^2 + \frac{\sigma_\phi^2}{2} + \frac{3\sigma_\phi^4}{4}\right)\sin^2(\omega\tau). \quad (6)$$

The functions $C_{x,x}(\tau)$ are the time-lagged autocovariances of either the phase ($x = \phi$) or amplitude ($x = \alpha$) modulations, and $\sigma_x^2 = C_{x,x}(0)$ are the corresponding variances. Note that higher-order terms in σ_ϕ^2 and σ_α^2 have been consistently neglected in (6).

A model for Γ is proposed, Γ_m, which includes variance from instrumental error and path delay corrections (σ_0^2), a trend [$\alpha_0^2\tau$, which might account for seasonality in the accuracy of $\mathbf{h}(\mathbf{x}, t)$ or the path delay corrections], first-order autoregressive processes characterized by variance σ_i^2 and time scale λ_i, and modulated periodic processes with amplitude A_i and frequency ω_i:

$$\Gamma_m(\tau)/2 = \sigma_0^2 + \alpha_0^2\tau + \sum_{i=1}^{2}\sigma_i^2[1 - \exp(-\tau/\lambda_i)] + \sum_{i=1}^{8}\gamma_i(\tau). \quad (7)$$

Submodels for the periodic processes, denoted γ_i of the form (6), include the dominant semidiurnal and diurnal tides (M_2, S_2, K_1, and O_1), three minor semidiurnal tides (N_2, μ_2, and L_2), and the J2 orbital repeat period. For reference, a reduced model shall be used below in which the nonstationary tides are neglected; it is given by

$$\Gamma_0(\tau)/2 = \sigma_0^2 + \alpha_0^2\tau + \sum_{i=1}^{2}\sigma_i^2[1 - \exp(-\tau/\lambda_i)] + \sum_{i=1}^{8}A_i^2[1 - \cos(\omega_i\tau)]. \quad (8)$$

Nonlinear least squares has been used to estimate the values $\lambda_1 = 3$ h and $\lambda_2 = 500$, time scales associated with the microscale and mesoscale temporal processes, respectively. Note the factor of ½ on the left-hand sides of (7) and (8), which is included so that the model coefficients correspond to SSH variance associated with the given process.

3. Results

Parameters in the above model are determined in a two-stage process. The first stage consists of neglecting the nonstationary tides and determining the α_0^2, σ_i^2, and A_i^2 parameters by least squares regression of Γ with the model Γ_0. In the second stage of analysis, the residual $\Gamma - \Gamma_0$ is high-pass filtered and demodulated at the frequencies of the dominant semidiurnal constituents to estimate the sum $C_{\phi,\phi} + C_{\alpha,\alpha}$ from the coefficient of the $\cos(\omega_i\tau)$ terms. Note that separate determinations of the $C_{\phi,\phi}$ and $C_{\alpha,\alpha}$ functions are not possible at this level of analysis.

Table 1 presents the linear regression coefficients obtained by ordinary least squares fitting of Γ_0 over the entire range of lags. The tidal coefficients represent stationary (phase locked) variance, which may be attributed either to barotropic tides not removed by the GOT4.10 model or to baroclinic tides. The amplitudes of the μ_2 and L_2 tides are anomalously large, which may be an indication of error in the GOT4.10 tidal model at these frequencies. The estimated uncertainty of the tidal coefficients is 0.02 cm^2.

A comparison of the values in Table 1 with the $\Gamma(\tau)$ function in Fig. 2b is instructive. The amplitude of the semidiurnal oscillation (½ of peak to peak) in the figure is approximately 2 cm^2, which corresponds to 1 cm^2 of tidal variance. The sum of the model coefficients associated with the semidiurnal band is 0.73 cm^2 (Table 1, A_1^2 through A_5^2). The difference between these values indicates that about 0.27 cm^2 variance is associated with the nonstationary semidiurnal tide. Note that this estimate is very sensitive to the amplitude of the semidiurnal oscillation inferred from Fig. 2b; a more precise estimate is made below.

Figure 3 illustrates the $\Gamma(\tau)$ function and the stationary model $\Gamma_0(\tau)$ for τ values covering three consecutive spring–neap cycles. For clarity, both sets of curves have been high-pass filtered for presentation purposes (48-h half-power point). Both Γ and Γ_0 exhibit modulations within an envelope of values. The modulations of Γ_0 are completely determined by the beating of the frequencies of the astronomical tide, while Γ includes deterministic modulations as well as noise.

The power spectral density of Γ and $\Gamma - \Gamma_0$ is shown in Fig. 4. The stationary model explains about 70% of the

TABLE 1. The $\Gamma_m(\tau)$ regression coefficients.

Coefficient	Process	Value (cm^2)
σ_0^2	Instrumental noise	4.3
α_0^2	Trend	-0.005 day^{-1}
σ_1^2	$\lambda_1 = 3$ h AR(1)	2.3
σ_2^2	$\lambda_2 = 40$ h AR(1)	2.2
A_1^2	M_2 tide (12.42 h)	0.34
A_2^2	S_2 tide (12.00 h)	0.11
A_3^2	N_2 tide (12.66 h)	0.07
A_4^2	μ_2 tide (12.87 h)	0.14
A_5^2	L_2 tide (12.19 h)	0.08
A_6^2	K_1 tide (23.93 h)	0.15
A_7^2	O_1 tide (25.82 h)	0.04
A_8^2	J2 repeat (9.9156 day)	0.23

variance in both the diurnal and semidiurnal bands. As can be seen from Fig. 3, the residual variance in the semidiurnal band appears at all lags. The peak in the residual spectrum is near 12.7 h, at a slightly longer period than the dominant M_2 tide, which motivated inclusion of the minor tides N_2, μ_2, and L_2 in Γ_m. A search for other minor tides resolvable within the 60-day lag window found none with signal-to-noise ratio greater than 2.

The time domain analysis cannot distinguish between barotropic and baroclinic tidal signals in SSH, and it is tacitly assumed that the tidal correction by GOT4.10 removes the majority of barotropic tidal variance from the SSH. The semidiurnal variance estimated from short lags ($1\,cm^2$) is definitely larger than the GOT4.10 error variance in deep water (Stammer et al. 2014), and it is almost certainly dominated by the internal tide. It is likely that the majority of the variance associated with the minor tides, μ_2 and L_2, is associated with the barotropic tide. The μ_2 frequency is identical to the frequency of the nonlinear shallow water overtide $2SM_2$, and its amplitude may be an indication of the size of this overtide in the deep ocean (R. D. Ray 2014, personal communication).

Next, characteristics of the nonstationary tide are identified by examining the semidiurnal band variance in the high-passed residual $\Gamma(\tau) - \Gamma_0(\tau)$. Figure 5 illustrates the semidiurnal band variance in this quantity as determined by a complex demodulation consisting of least squares regression of $\Gamma(\tau) - \Gamma_0(\tau)$ onto $-\cos(\omega_1 t)$ (M_2) and $-\cos(\omega_6 t)$ (K_1) within overlapping 48-h data windows (circles). Figure 5 also shows demodulates from analysis of 360-h windows (solid line), which removes the spring–neap variability present in the 48-h window demodulates. The amplitude of the demodulate near zero lag is approximately $0.33\,cm^2$, slightly larger

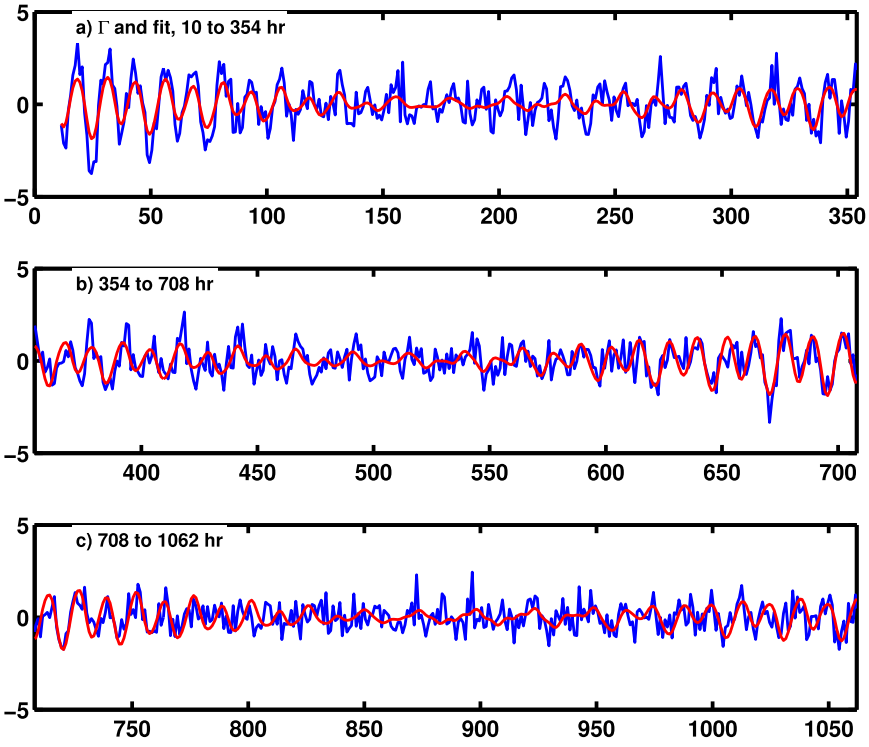

FIG. 3. High-passed $\Gamma(\tau)$ and $\Gamma_0(\tau)$. (a)–(c) The high-passed $\Gamma(\tau)$ function (blue) for three different ranges of the lag τ; each a complete spring–neap cycle (354.4 h). The high-passed $\Gamma_0(\tau)$ function (red) contains harmonics at the M_2, S_2, K_1, and O_1 and other tidal frequencies; therefore, it is not exactly periodic over the spring–neap cycle.

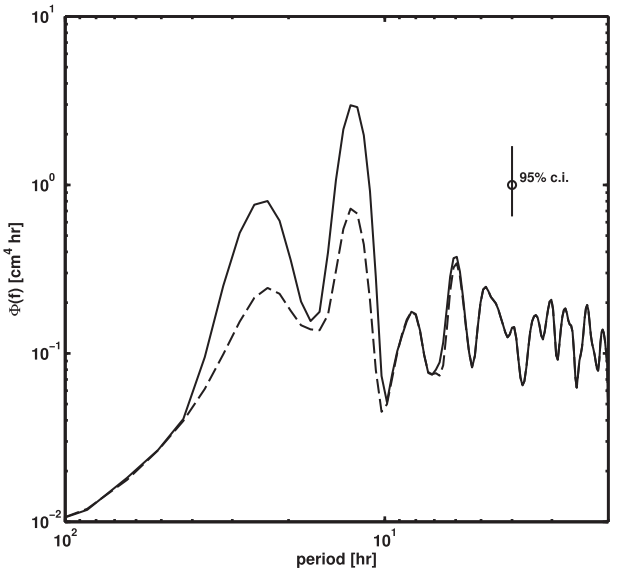

FIG. 4. Power spectral density of high-passed $\Gamma(\tau)$ (solid) and nonstationary residual, $\Gamma(\tau) - \Gamma_0(\tau)$ (dashed). The tidal harmonics explain approximately 70% of the variance in both the diurnal and semidiurnal bands. The spectrum was estimated using Bartlett's method with the Tukey window over 100-h segments; each estimate contains approximately 36 degrees of freedom.

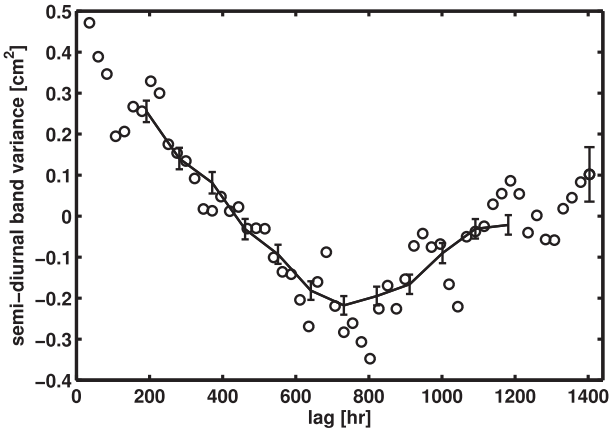

FIG. 5. Complex demodulation of semidiurnal band variance. Complex demodulation of the high-passed semidiurnal-band variance of the residual $\Gamma(\tau) - \Gamma_0(\tau)$ at the M_2 and K_1 frequencies is performed within 48-h windows (circles; error bar shown on last demodulate only) and within 360-h windows (solid line; error bars shown). Because of the overlap of data windows, every fifth demodulate is statistically independent; K_1 demodulates are of marginal statistical significance and are not shown.

than the estimate obtained above by comparing Fig. 2b and Table 1, which is about 30% of the total (coherent plus incoherent) semidiurnal variance. The demodulate, which is an estimate of $C_{\phi,\phi} + C_{\alpha,\alpha}$, decays to 0 near 400 h, indicating that the nonstationary internal tide becomes incoherent within 17 days. The demodulate indicates negative correlation for lags from 400 to 1000 h (17–35 days), which may be related to the time scale of refraction by mesoscale eddies. A westward-propagating mesoscale SSH anomaly propagating at $6\,\mathrm{cm\,s^{-1}}$ (Chelton and Schlax 1996) would take about 700 h to cross a 150-km-wide internal tide beam. Unfortunately, the signal-to-noise ratio of the K_1 demodulate is too low to make any conclusions about nonstationary diurnal variability.

4. Discussion

The demodulates shown in Fig. 5 indicate that the nonstationary internal tide rapidly decorrelates as it propagates through the deep ocean. Based on the present analysis in the time domain, approximately 30% of the semidiurnal internal tide SSH variance is nonstationary. This result is somewhat higher than estimated by other methods (Dushaw et al. 1995; Chiswell 2002; Ray and Zaron 2011; Dushaw et al. 2011), although the present work is apparently the first assessment of a near-global average.

One attribute of the internal tide highlighted in previous observational and modeling studies is the spatial inhomogeneity of the associated SSH field (e.g., Simmons et al. 2004). The present analysis has relied exclusively on second-order statistics, that is, an analysis of variance, which, by definition, gives higher weight to those regions with larger SSH amplitude. To examine the possibility of bias, a parallel analysis was conducted using a first-order statistic analogous to $\Gamma(\tau)$, the mean absolute deviation (not shown); however, no significant differences in tidal variance were found.

Another aspect of spatial variability is connected with the dynamics of internal tide generation and propagation. For example, the diurnal tides are not expected to propagate poleward of the turning latitude where the waves are subinertial (e.g., approximately 30° for K_1). Computing the Γ statistic separately for regions poleward and equatorward of 30° latitude finds large differences in properties of diurnal tides. The stationary K_1 variance is $0.08\,\mathrm{cm^2}$ poleward of 30° and $0.23\,\mathrm{cm^2}$ equatorward of 30° (cf. Table 1). Thus, the statistical approach taken here broadly agrees with our understanding of tidal dynamics. Taking this approach further to develop a spatially resolved picture is difficult, though, as it involves a trade-off between sampling errors, which increase as the number of data points is reduced by subsetting and spatial resolution. This is an area of ongoing efforts.

Model-based studies of the generation and propagation of nonstationary tides have been conducted previously. A result that is directly comparable with the

present work is the study of Zaron and Egbert (2014), in which the stationary and nonstationary internal tide variance was mapped near Hawaii. They found that 20% of the M_2 internal tide variance is nonstationary in the vicinity of the Hawaiian ridge, as a result of scattering by the mesoscale, although, this value was likely biased low by the smoothed representation of the mesoscale used in their model. Shriver et al. (2014) conducted a global study utilizing a concurrent simulation of tides, wind, and thermohaline forcing, but the conditional averaging procedures used in that paper make detailed comparisons with the present work difficult. Away from generation sites, they found a wide range for the ratio of nonstationary to total internal tide variance, which appears to be consistent with the value obtained here.

The temporal structure function presented in Fig. 2 is a summary of oceanic variability that complements previous analyses in the (spatial) wavenumber domain (Fu 1983; LeTraon et al. 1990; Stammer 1997; LeTraon et al. 2008; Xu and Fu 2011). It shows that the present altimeter constellation is capable of mapping the ocean mesoscales at time scales greater than 150 h. It also indicates that about 10 cm^2 of SSH variance remains to be mapped at shorter time scales. This sub-6-day variance may be partitioned into 2.5 cm^2 of very high-frequency variability (5-h time scale and shorter), 2.5 cm^2 of tidal variance, and about 5 cm^2 of other SSH variance, which includes unresolved mesoscale and submesoscale variability, topographic Rossby and Kelvin waves, and other gravity waves (note that these SSH variance estimates correspond to ½ of the structure function values shown in Fig. 2).

5. Conclusions

J2 and C2 crossover data have been used to compute the second-order structure function of SSH for data collocated in space but separated in time. The structure function partitions the SSH variance according to time scale in a manner analogous to the frequency power spectrum, but without the need for evenly spaced time series. For analysis of internal tidal signals, precision was enhanced by subtracting off the known SSH signal (the barotropic tide and the slowly evolving mesoscale) and averaging in space, between ±55° latitude, and time, from 1 January 2010 to 30 May 2014.

The tidal variance present in the structure function was used to compute, for the first time, near-global averages of the amplitudes of the stationary and nonstationary internal tides. Within the semidiurnal band, for which highly accurate prior models are available to remove the barotropic tide, about 1-cm^2 SSH variance is found, the majority of which may be attributed to the internal tide. For the dominant M_2 tide, about 30% of the total internal tide variance is found to be nonstationary, and it decorrelates from the tidal forcing on a time scale of 400 h. A significant signal of 0.14 ± 0.02 cm^2 is found in the structure function associated with the μ_2 (alternately, $2SM_2$) frequency, and this suggests that previously neglected minor tides and overtides ought to be included in future empirical barotropic tide models. The averaged properties of the internal tide inferred in this study place much-needed observational constraints on global tide and mesoscale-resolving models that are increasingly being used for ocean prediction and studies of climate dynamics.

The results obtained also suggest a strategy for predicting the nonstationary low-mode internal tide, as will be needed for detiding data from the future SWOT wide-swath altimeter mission. The temporal filtering scale of the mesoscale signal in the Ssalto–Duacs (AVISO) gridded SSH maps is approximately 150 h, and this is significantly shorter than the 400 h decorrelation time of the nonstationary semidiurnal tide. Because a significant fraction of the time-variable mesoscale signal is resolved at time scales of shorter than the decorrelation time of the tide, it may be feasible to resolve much of the internal tide variability in a data-assimilative mesoscale-resolving model, provided the model is capable of producing the correct phase-speed modulations associated with the mesoscale SSH. Once demonstrated, such a capability would enhance the efficacy of tidal corrections in the future.

Acknowledgments. Satellite altimeter data used in this study were extracted from the RADAR Altimetry Database System (RADS; http://rads.tudelft.nl/rads/rads.shtml). The mesoscale SSH fields, $\mathbf{h}(\mathbf{x}, t)$, were produced by Ssalto/Duacs and distributed by AVISO, with support from Cnes (http://www.aviso.altimetry.fr/duacs/). This project was supported by NASA Award NNX09AF20G (Ocean Surface Topography Science Team). The author acknowledges and appreciates the constructive comments of two anonymous reviewers, one of whom suggested looking for a relationship between diurnal modulations and the diurnal turning latitude now mentioned at the end of section 3.

REFERENCES

Barnett, T. P., and R. L. Bernstein, 1975: Horizontal scales of midocean internal tides. *J. Geophys. Res.,* **80,** 1962–1964, doi:10.1029/JC080i015p01962.

Casella, G., and R. L. Berger, 2002: *Statistical Inference*. 2nd ed., Duxbury/Thomson Learning, 660 pp.

Chavanne, C., P. Flament, D. Luther, and K. Gurgel, 2010: The surface expression of semidiurnal internal tides near a strong

source at Hawaii. Part II: Interactions with mesoscale currents. *J. Phys. Oceanogr.,* **40,** 1180–1200, doi:10.1175/2010JPO4223.1.

Chelton, D. B., and M. G. Schlax, 1996: Global observations of oceanic Rossby waves. *Science,* **272,** 234–238, doi:10.1126/science.272.5259.234.

Chiswell, S. M., 2000: Tidal energetics over the Chatham Rise, New Zealand. *J. Phys. Oceanogr.,* **30,** 2452–2460, doi:10.1175/1520-0485(2000)030<2452:TEOTCR>2.0.CO;2.

——, 2002: Energy levels, phase, and amplitude modulation of the baroclinic tide off Hawaii. *J. Phys. Oceanogr.,* **32,** 2640–2651, doi:10.1175/1520-0485-32.9.2640.

Dushaw, B. D., P. F. Worcester, B. D. Cornuelle, B. M. Howe, and D. S. Luther, 1995: Baroclinic and barotropic tides in the central North Pacific Ocean determined from long-range reciprocal acoustic transmissions. *J. Phys. Oceanogr.,* **25,** 631–647, doi:10.1175/1520-0485(1995)025<0631:BABTIT>2.0.CO;2.

——, ——, and M. A. Dzieciuch, 2011: On the predictability of mode-1 internal tides. *Deep-Sea Res. I,* **58,** 677–698, doi:10.1016/j.dsr.2011.04.002.

Frisch, U., 1995: *Tubulence: The Legacy of A. N. Kolmogorov*. Cambridge University Press, 296 pp.

Fu, L., 1983: On the wave number spectrum of oceanic mesoscale variability observed by the SEASAT altimeter. *J. Geophys. Res.,* **88,** 4331–4341, doi:10.1029/JC088iC07p04331.

Gill, A. E., 1982: *Atmosphere-Ocean Dynamics*. Academic Press, 662 pp.

Klymak, J. M., R. Pinkel, and L. Rainville, 2008: Direct breaking of the internal tide near topography: Kaena Ridge, Hawaii. *J. Phys. Oceanogr.,* **38,** 380–399, doi:10.1175/2007JPO3728.1.

LeProvost, C., 2001: Ocean tides, in *Satellite Altimetry and Earth Sciences,* L.-L. Fu and A. Cazenave, Eds., International Geophysics Series, Vol. 69, Academic Press, 267–303.

LeTraon, P., M. C. Rouquet, and C. Boissier, 1990: Spatial scales of mesoscale variability in the North Atlantic as deduced from Geosat data. *J. Geophys. Res.,* **95,** 20 267–20 285, doi:10.1029/JC095iC11p20267.

——, F. Nadal, and N. Ducet, 1998: An improved mapping method of multi-satellite altimeter data. *J. Atmos. Oceanic Technol.,* **15,** 522–534, doi:10.1175/1520-0426(1998)015<0522:AIMMOM>2.0.CO;2.

——, P. Klein, B. L. Hua, and G. Dibarboure, 2008: Do altimeter spectra agree with the interior or surface quasigeostrophic theory? *J. Phys. Oceanogr.,* **38,** 1137–1142, doi:10.1175/2007JPO3806.1.

Magaard, L., and W. D. McKee, 1973: Semidiurnal tidal currents at site D. *Deep-Sea Res. Oceanogr. Abstr.,* **20,** 997–1009, doi:10.1016/0011-7471(73)90071-5.

Naeije, M., E. Doornbos, L. Mathers, R. Scharroo, E. Schrama, and P. Visser, 2002: Radar altimeter database system: Exploitation and extension (RADSxx). Tech. Rep. 02-06, NUSP-2 project 6.3/IS-66, Delft Institute for Earth-Oriented Space Research, Delft, Netherlands, 99 pp.

Park, J.-H., and D. Farmer, 2013: Effects of kuroshio intrusions on nonlinear internal waves in the South China Sea during winter. *J. Geophys. Res.,* **118,** 7081–7094, doi:10.1002/2013JC008983.

Picaut, J., A. J. Busalacchi, M. J. McPhaden, L. Gourdeau, F. I. Gonzalez, and E. C. Hackert, 1995: Open-ocean validation of TOPEX/POSEIDON sea level in the western equatorial Pacific. *J. Geophys. Res.,* **100,** 25 109–25 127, doi:10.1029/95JC02128.

Picot, N., S. Desai, J. Figa-Saldana, and R. Scharroo, 2014: Jason-2 Version 'D' geophysical data records: Public release. AVISO, accessed 1 December 2014. [Available online at http://www.aviso.oceanobs.com/fileadmin/documents/data/tools/JA2_GDR_D_release_note.pdf.]

Rainville, L., and R. Pinkel, 2006: Propagation of low-mode internal waves through the ocean. *J. Phys. Oceanogr.,* **36,** 1220–1236, doi:10.1175/JPO2889.1.

Ray, R. D., and G. T. Mitchum, 1996: Surface manifestation of internal tides generated near Hawaii. *Geophys. Res. Lett.,* **23,** 2101–2104, doi:10.1029/96GL02050.

——, and D. A. Byrne, 2010: Bottom pressure tides along a line in the southeast Atlantic Ocean and comparisons with satellite altimetry. *Ocean Dyn.,* **60,** 1167–1176, doi:10.1007/s10236-010-0316-0.

——, and E. D. Zaron, 2011: Non-stationary internal tides observed with satellite altimetry. *Geophys. Res. Lett.,* **38,** L17609, doi:10.1029/2011GL048617.

Rudnick, D. L., and Coauthors, 2003: From tides to mixing along the Hawaiian Ridge. *Science,* **301,** 355–357, doi:10.1126/science.1085837.

Shriver, J. F., J. G. Richman, and B. K. Arbic, 2014: How stationary are the internal tides in a high-resolution global ocean circulation model? *J. Geophys. Res.,* **119,** 2769–2787, doi:10.1002/2013JC009423.

Siedler, G., 1991: Barotropic and baroclinic tidal currents in the eastern basins of the North Atlantic. *J. Geophys. Res.,* **96,** 22 259, doi:10.1029/91JC02319.

Simmons, H. L., R. W. Hallberg, and B. K. Arbic, 2004: Internal wave generation in a global baroclinic tide model. *Deep-Sea Res. II,* **51,** 3043–3068, doi:10.1016/j.dsr2.2004.09.015.

Stammer, D., 1997: Global characteristics of ocean variability estimated from regional TOPEX/POSEIDON altimeter measurements. *J. Phys. Oceanogr.,* **27,** 1743–1769, doi:10.1175/1520-0485(1997)027<1743:GCOOVE>2.0.CO;2.

——, and Coauthors, 2014: Accuracy assessment of global barotropic ocean tide models. *Rev. Geophys.,* **52,** 243–282, doi:10.1002/2014RG000450.

Weisberg, R. H., D. Halpern, T. Y. Tang, and S. M. Hwang, 1987: M_2 tidal currents in the eastern equatorial Pacific Ocean. *J. Geophys. Res.,* **92,** 3821–3826, doi:10.1029/JC092iC04p03821.

Xu, Y., and L. Fu, 2011: Global variability of the wavenumber spectrum of oceanic mesoscale turbulence. *J. Phys. Oceanogr.,* **41,** 802–809, doi:10.1175/2010JPO4558.1.

Zaron, E. D., and G. D. Egbert, 2014: Time-variable refraction of the internal tide at the Hawaiian Ridge. *J. Phys. Oceanogr.,* **44,** 538–557, doi:10.1175/JPO-D-12-0238.1.

Zhao, Z., M. H. Alford, J. Girton, T. M. Johnston, and G. Carter, 2011: Internal tides around the Hawaiian Ridge estimated from multisatellite altimetry. *J. Geophys. Res.,* **116,** C12039, doi:10.1029/2011JC007045.

Zilberman, N. V., M. A. Merrifield, G. S. Carter, D. S. Luther, M. D. Levine, and T. J. Boyd, 2011: Incoherent nature of M_2 internal tides at the Hawaiian Ridge. *J. Phys. Oceanogr.,* **41,** 2021–2036, doi:10.1175/JPO-D-10-05009.1.